Slotted Hemispherical Resonators for 3-D Printed Waveguide Filters With Extended Spurious-Free Stopbands

JIN LI [1,2]**, (Member, IEEE), KAI-DONG HONG** [1]**, AND TAO YUAN** [1,3]

[1]Guangdong Provincial Mobile Terminal Microwave and Millimeter-Wave Antenna Engineering Research Center, College of Electronics and Information Engineering, Shenzhen University, Shenzhen 518060, China
[2]State Key Laboratory of Millimeter Waves, Nanjing 210096, China
[3]ATR National Key Laboratory of Defense Technology, College of Electronics and Information Engineering, Shenzhen University, Shenzhen 518060, China

Corresponding author: Tao Yuan (yuantao@szu.edu.cn)

ABSTRACT This paper presents a comprehensive study on a new family of slotted hemispherical resonators and their applications in waveguide bandpass filters (BPFs) to extend the spurious-free stopbands. The proposed scheme focuses on suppressing unwanted spurious modes in the air-filled hemispherical resonators by adding functional slots to the metallic cavity shells. The spurious TM_{2m1} and TE_{101} modes in the hemispherical resonators are effectively suppressed by interrupting the surface current with slots, without significantly degrading the unloaded quality factor of the fundamental TM_{101} mode. Resonant modes in the slotted hemispherical resonators are analyzed. Design, fabrication, and measurement of X-band proof-of-concept waveguide BPFs based on slotted hemispherical resonators are expounded. Each filter is monolithically prototyped by employing metallic additive manufacturing technology. The filters demonstrate good passband performance—average insertion loss: 0.6–1.1 dB, frequency shift: 0.9%–1%, and return loss: >20 dB, and more significantly extended stopbands with spurious-free frequency ratios of >1.8:1 and stopband rejections over 36 dB.

INDEX TERMS Additive manufacturing, direct metal laser sintering, slotted hemispherical resonator, spurious-free stopband, spurious suppression, waveguide filter.

I. INTRODUCTION

High-performance waveguide/cavity-based filtering components have been extensively used in microwave and millimeter-wave frontend hardware [1]. These circuits usually demand high-quality-factor (high-Q) cavity resonators because the high Q gives small loss and high power capacity. Air-filled metallic rectangular and cylindrical cavities are two types of high-Q resonators that have been commonly used to date in filters and multiplexers [2]–[4]. They can be readily fabricated with conventional subtractive manufacturing technology such as computer-numerical controlled (CNC) milling. The other type of resonator with a much higher intrinsic unloaded quality factor (Q_u) under an identical building material and a same resonant frequency is the spherical

The associate editor coordinating the review of this manuscript and approving it for publication was Xiu Yin Zhang.

cavity. However, it is not easy to fabricate spherical cavities precisely and cost-efficiently using CNC milling. This limits practical engineering applications of spherical resonators. In the past, spherical cavities have been applied to multi-mode bandpass filters (BPFs) (e.g., [5]), where the packages of the filters need to be split into several parts for milling and then assembled with many screws. Unfortunately, this would introduce tolerance degrading RF performance of the filters.

In recent years, additive manufacturing (AM, also known as 3-D printing) technology has been introduced to the fabrication of microwave devices enabling fast prototyping of sophisticated geometries at reduced expenses [6]–[10]. This makes fabrication of spherical-resonator-based circuits more convenient. In [11]–[13], spherical resonators are 3-D printed to construct microwave bandpass filters (BPFs). The spherical resonator BPF in [11] exhibits an ultra-low passband insertion loss (IL) due to the high Q_u. However, the stopband

performance of the filter is degraded because the spurious modes in the spherical resonator are spectrally close to the fundamental mode. The stopband rejection of the filter can be improved by using either the 90°-twisted coupling geometry [11], [12] that minimizes coupling strength of the spurious TM_{211} mode, or the hemispherical resonator that features a much reduced number of spurious modes [14], [15]. However, the stopband bandwidth is still limited by the spurious resonances because in the aforementioned filter demonstrations spurious modes in the constituent resonators are not suppressed. A method to intrinsically suppress the spurious modes can be geometrically shaping the cavities. For example, the waveguide filters in [16] and [17] are composed of mathematically defined super-ellipsoid resonators and demonstrate excellent passband and stopband performances. Except for [16] and [17], there is little work in spurious suppression for 3-D printed filters.

In this work, the other approach to effectively suppress the spurious modes by slotting the cavity resonator is proposed and a new class of air-filled slotted hemispherical resonators is introduced. The suppression is realized by interrupting surface current of the unwanted spurious modes via properly slotting the hemispherical cavity. This significantly extends the stopband of the hemispherical resonator BPF. The slot is opened not to seriously impact the fundamental-mode Q_u and the fundamental-mode passband of the filter is thus not interfered. It is noteworthy that the filter in [13] was designed with perforated dual-mode spherical resonators and its feeding waveguides were also slotted. Similarly, slots are also adopted to 3-D printed rectangular and cylindrical waveguide filters in [18]–[20]. However, they were used mainly to facilitate the metal electroplating process by offering pathways through the cavities for the plating solution. Such slots do not improve any RF performance of the filter. The emphasis of this work is, therefore, enhancing the spurious-free region by putting slots in the structure aiming to maximize the suppression. Significantly extended spurious-free stopbands with suppressed resonances have been achieved as compared with previous work. 3-D printing technology allows such complex filter geometries to be fabricated monolithically, eliminating the assembly tolerance and the use of any fastening element.

The content of this paper is organized as follows. The structure and resonant modes of the slotted hemispherical resonator are analyzed in Section II. The RF design of several proof-of-concept X-band slotted hemispherical resonator waveguide filters is presented in Section III. The fabrication process for monolithically 3-D-printing the filters is introduced in Section IV. The measurement and characterization of the 3-D printed filters are discussed in Section V.

II. SLOTTED HEMISPHERICAL RESONATORS
A. RESONANT MODE ANALYSIS
To clearly describe the principle of spurious suppression of this work, the surface current distribution for the fundamental TM_{101} mode and several spurious modes of interest
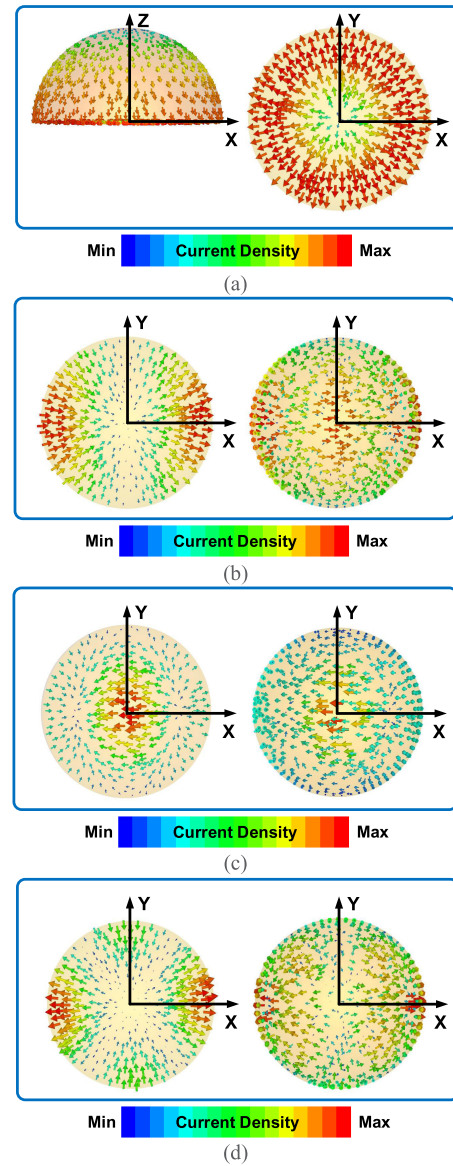

FIGURE 1. Surface current distribution of several resonant modes in a non-slotted hemispherical cavity. (a) The fundamental TM_{101} mode (left/right: side/bottom face). (b) The first spurious TM_{2m1} mode (left/right: bottom/top face). (c) The second spurious TE_{101} mode (left/right: bottom/top face). (d) The third spurious TM_{3m1} mode (left/right: bottom/top face).

in a non-slotted hemispherical cavity has been illustrated in Fig. 1. When an air-filled hemispherical cavity is fed with a rectangular waveguide, as demonstrated in [14] and [15], the first, second, and third excited spurious modes are TM_{2m1}, TE_{101}, and TM_{3m1} modes. The eigenmode frequencies of these spurious modes are determined by the radius of the hemisphere, and can be analytically calculated using (1)–(3)

$$f_{TM2m1} = \frac{\omega_{TM2m1}}{2\pi} = \frac{y_{21}}{2\pi r \sqrt{\mu\varepsilon}} = \frac{3.870}{2\pi r \sqrt{\mu\varepsilon}}, \quad (1)$$

$$f_{TE101} = \frac{\omega_{TE101}}{2\pi} = \frac{x_{11}}{2\pi r \sqrt{\mu\varepsilon}} = \frac{4.493}{2\pi r \sqrt{\mu\varepsilon}}, \quad (2)$$

$$f_{TM3m1} = \frac{\omega_{TM3m1}}{2\pi} = \frac{y_{31}}{2\pi r \sqrt{\mu\varepsilon}} = \frac{4.973}{2\pi r \sqrt{\mu\varepsilon}}, \quad (3)$$

where ω_{TM2m1}, ω_{TE101}, and ω_{TM3m1} are the corresponding angular frequencies, r is the radius variable of the cavity with a unit in millimeter, and the roots y_{21}, x_{11}, and y_{31} of the eigenvalue equation equal to 3.870, 4.493, and 4.973 for TM_{2m1}, TE_{101}, and TM_{3m1} modes, respectively [21]. The parameters μ and ε are permeability and permittivity of the dielectric filled in the cavity. In free space, (1)–(3) yield

$$f_{TM2m1} \approx \frac{1.8478 \times 10^{11}}{r} (Hz), \quad (4)$$

$$f_{TE101} \approx \frac{2.1452 \times 10^{11}}{r} (Hz), \quad (5)$$

$$f_{TM3m1} \approx \frac{2.3744 \times 10^{11}}{r} (Hz). \quad (6)$$

For example, with a TM_{101}-mode frequency of 10 GHz, i.e., in case of $r = 13.1$ mm, f_{TM2m1}, f_{TE101}, and f_{TM3m1} equal to about 14.1, 16.37, and 18.13 GHz, respectively. This was verified by performing electromagnetic (EM) simulation using the eigenmode solver in Computer Simulation Technology (CST) Studio Suite [22]. The eigenmode-simulated and numerically calculated resonant frequencies are graphically compared in Fig. 2 and show excellent agreement.
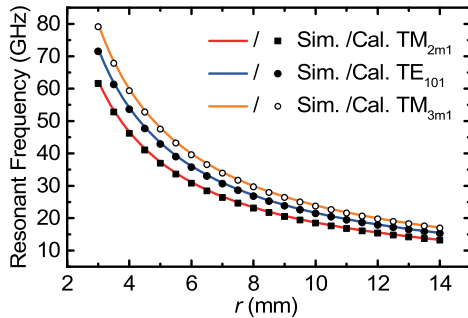

FIGURE 2. Eigenmode resonant frequencies of the spurious modes in a non-slotted hemispherical cavity.

The principle of spurious suppression of this work is interfering surface current of the unwanted spurious modes with slots on the cavity shell whilst keeping surface current of the fundamental mode intact. The spurious modes with surface current interrupted radiate through the slots. As can be seen in Fig. 1, at the top of the hemisphere, the surface current density reaches the maximum for the TM_{2m1} and TE_{101} modes whereas the minimum for the TM_{101} mode. If a slot is properly opened in this area, the TM_{2m1} and TE_{101} modes can be seriously interfered and the impact of slotting on the TM_{101} mode can be minimized. Similarly, in the center area of the bottom face, the surface current reaches the minimum for the TM_{101} and TM_{2m1} modes whereas the maximum for the TE_{101} mode. If a slot is properly opened on the bottom face, the TE_{101} mode can be suppressed without interfering the TM_{101} and TM_{2m1} modes. It should be mentioned that the TM_{3m1} mode has overlapping components of the surface

current to the TM_{101} mode. Therefore, suppressing TM_{3m1} and the modes beyond without interfering the TM_{101} mode is difficult and is out of scope of this work.

B. SUPPRESSION OF SPURIOUS MODES
In order to maximize the suppression of the TM_{2m1} mode, a rectangular slot is introduced along the y-axis on the top shell of the hemispherical cavity, as illustrated in Fig. 3. The slot is placed in a longitudinal direction perpendicular to the current orientation of the TM_{2m1} mode on the top shell. Note that the slot orientation is also perpendicular to the current direction of the TE_{101} mode in this area. Therefore, both spurious modes can be suppressed simultaneously.
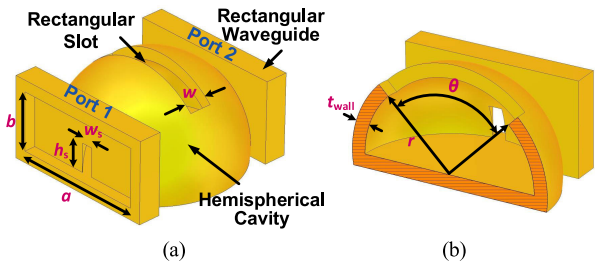

FIGURE 3. A geometrical configuration of a hemispherical cavity with a rectangular slot on the top shell. (a) A complete simulation model of the waveguide-side-fed resonator. (b) The slot profile.

The spurious suppression was verified by investigating power transmission response of the top-slotted resonator under weak external couplings. The waveguide side-feeding structure in Fig. 3 with a coupling aperture size of $w_s = 2$ mm and $h_s = 5$ mm [as labeled in Fig. 3(a)] was used for EM simulation in CST. The slotted hemispherical cavity was designed with a TM_{101}-mode frequency of 10 GHz and was mated to a pair of WR-90 waveguides, where the following dimensions were fixed in the simulation: $a = 22.86$ mm, $b = 10.16$ mm, $r = 13.1$ mm, and $t_{wall} = 2$ mm. The suppression is controlled by the width w and angle θ [as labeled in Fig. 3(b)] of the slot. The EM-simulated transmission coefficient of the weakly fed resonator under different slot dimensions is plotted in Fig. 4. The slot angle θ is initialized to be 90° according to the area that the spurious-mode current is concentrated in. As can be seen in Fig. 4(a), the suppression of the TM_{2m1} and TE_{101} modes is enhanced simultaneously as the width w is increased. When $w \geq 4$ mm, the spurious resonances at 14.1 and 16.37 GHz are fully eliminated. As expected, the TM_{101} and TM_{3m1} modes are not much influenced by the slot. The simulated result in Fig. 4(b) indicates that an even larger angle ($\theta > 90°$) of the slot does not improve any spurious suppression. However, the suppression is degraded as θ is reduced to 30° because under such circumstance the slot is too short to interrupt the current sufficiently.

In order to quantify the influence of slotting on the loss of the resonator, the TM_{101}-mode Q_u of the resonator under different slot dimensions was investigated. The simulated Q_u is plotted in Fig. 5. In the simulation, the cavity boundary was set as copper with an electrical conductivity of 5.96×10^7 S/m
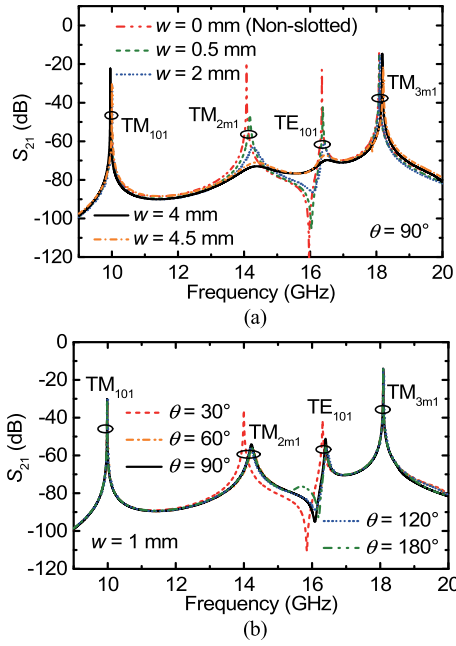
FIGURE 4. EM-simulated power transmission response of the weakly fed top-slotted hemispherical resonator. (a) The transmission coefficient (S_{21}) under different slot widths. (b) The transmission coefficient (S_{21}) under different slot angles.
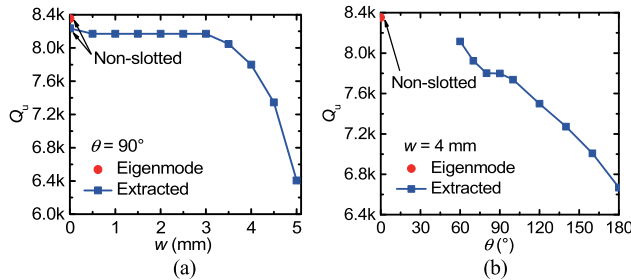

FIGURE 5. Simulated TM_{101}-mode Q_u of the top-slotted hemispherical resonator under different slot dimensions. (a) Q_us versus slot widths. (b) Q_us versus slot angles.

and the Q_u values were extracted from the S_{21} parameter of the weakly fed resonator using the method outlined in [23]. The result in Fig. 5 shows that the Q_u is reduced with the increase of θ and can be controlled almost unchanged in a certain range of w. Therefore, by trading off the Q_u and suppression a group of parameters, i.e., $w = 4$ mm and $\theta = 90°$, for the rectangular slot on the top face, was finalized for the filter design in Section III.

A further quantitative comparison in the conductor quality factor (Q_c) and radiation quality factor (Q_r) of the slotted hemispherical resonator was accomplished by simulation as follows. The loaded quality factor (Q_L) of the slotted hemispherical resonator in free space can be expressed as [23]

$$\frac{1}{Q_L} = \frac{1}{Q_e} + \frac{1}{Q_c} + \frac{1}{Q_r}, \tag{7}$$

where Q_e is the external quality factor associated with the small coupling aperture between the feeding rectangular

waveguide and the resonator. Note that in (7) the Q_L can be extracted directly from the simulated S_{21} parameter, the Q_e is determined by the feeding aperture size, and the Q_r is determined by the slot configuration. Firstly, to find the Q_e, a non-slotted hemispherical resonator with the feeding aperture size of 2 mm × 5 mm was used. In this scenario, the cavity boundary was set as a perfect electrical conductor (PEC), hence there would be no radiation loss or conductor loss. This makes reciprocals of both Q_c and Q_r zero. From (7) this yields $Q_L = Q_e$, which by simulation turns out to be about 2.63×10^5. Then, the slotted resonator was simulated with a PEC boundary. In this case, (7) turns into (8)

$$\frac{1}{Q_L} = \frac{1}{Q_e} + \frac{1}{Q_r}, \tag{8}$$

and the Q_L value extracted from the simulated S_{21} is about 8.85×10^4. Using (8) and the previously calculated Q_e for the non-slotted PEC resonator, the Q_r value was calculated to be about 1.33×10^5. Next, the cavity boundary material was changed to copper and the simulation of the slotted resonator produced a Q_L value of 7574. Having the values of Q_L, Q_e, and Q_r in (7) allows the calculation of Q_c, resulting in a Q_c value of 8284. This approximation allows us to conclude that the Q_r has virtually no influence on the TM_{101} mode because of the large difference in the Q values and $Q_c << Q_r$.

In addition, the TE_{101} mode can be suppressed independently using a rectangular slot on the bottom shell of the hemispherical cavity. An exemplified geometry of the bottom-slotted hemispherical resonator with feeding waveguides is illustrated in Fig. 6. The slot is opened along the symmetrical line of the bottom face and is perpendicular to the current orientation of the TE_{101} mode in this area. In this way, surface current of the TE_{101} mode is significantly interfered but the rest modes are not disturbed.
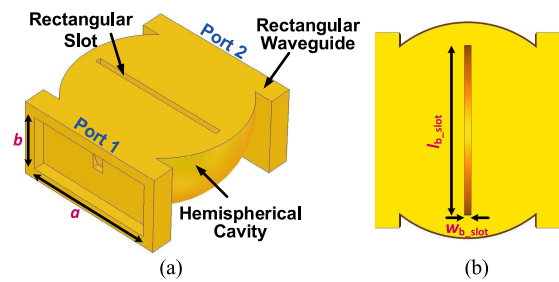

FIGURE 6. A geometrical configuration of a hemispherical cavity with a rectangular slot on the bottom shell. (a) A complete simulation model of the waveguide-side-fed resonator. (b) The slotted bottom face.

The simulated power transmission coefficient and the TM_{101}-mode Q_u of the weakly fed bottom-slotted hemispherical resonator under different slot dimensions are plotted in Figs. 7 and 8, respectively. According to the current density in Fig. 1(c), the length l_{b_slot} of the bottom slot was initialized to be 25 mm, approaching the diameter of the hemisphere. In this case, as shown in Fig. 7(a), the TE_{101} mode can be suppressed with a very narrow bottom slot, e.g., $w_{b\_slot} = 0.5$ mm, and the suppression is enhanced with the increase
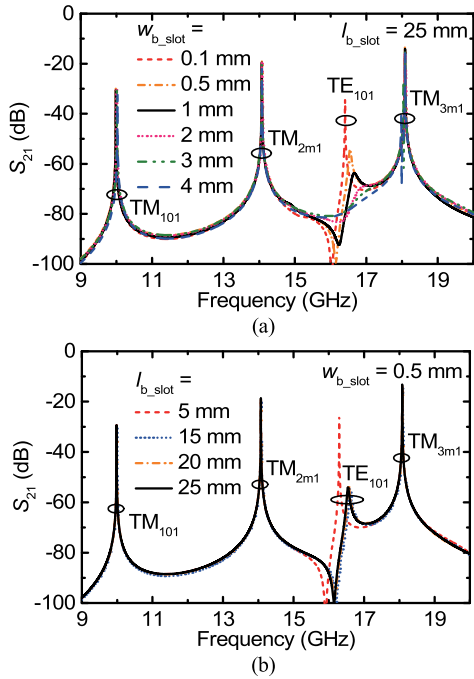
FIGURE 7. EM-simulated power transmission response of the weakly fed bottom-slotted hemispherical resonator. (a) The transmission coefficient (S_{21}) under different slot widths. (b) The transmission coefficient (S_{21}) under different slot lengths.
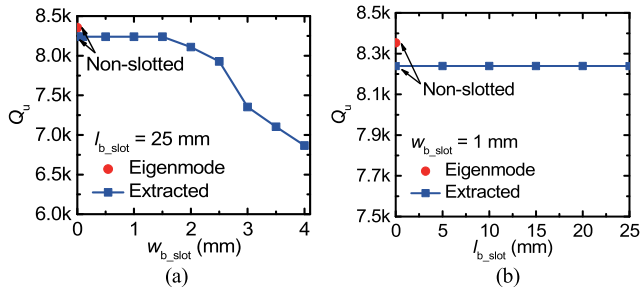

FIGURE 8. Simulated TM_{101}-mode Q_u of the bottom-slotted hemispherical resonator under different slot dimensions. (a) Q_us versus slot widths. (b) Q_us versus slot lengths.

of w_{b_slot} until w_{b_slot} reaches 4 mm. On the other hand, with a fixed w_{b_slot}, the suppression is not much degraded until l_{b_slot} is decreased to 5 mm, as shown in Fig. 7(b). Little interference is brought to the other modes when varying the bottom slot dimensions. The simulated result in Fig. 8 shows that the Q_u of the bottom-slotted resonator can be controlled close to the Q_u of the non-slotted resonator in the range of $w_{b\_slot} \leq 1.5$ mm, and is not much influenced by l_{b_slot} in this range. A group of appropriate slot dimensions can be selected as $w_{b\_slot} = 1.5$ mm and $l_{b\_slot} = 25$ mm taking into account the Q_u and suppression.

Using the selected slot dimensions and the same aperture in Fig. 3 for weak external couplings, the simulated Q_r and Q_c of the bottom-slotted hemispherical resonators were obtained as 2.30×10^6 and 8269, respectively. This again shows that $Q_c << Q_r$ and indicates negligible influence of the bottom slot on the TM_{101} mode.

It is also known from Figs. 4 and 7 that the proposed slot configurations have negligible influence on the resonant frequency of the fundamental TM_{101} mode. This influence is further quantified by simulation and the result is plotted in Fig. 9. In Fig. 9, the parameter Δf_r is defined as the relative resonant frequency shift and is calculated with reference to the simulated resonant frequency of the TM_{101} mode in a non-slotted hemispherical resonator. The calculated absolute values of Δf_r are less than 0.5% and 0.8% for the top-slotted and bottom-slotted resonators, respectively. In the filter design, these small frequency shifts are compensated by adjusting the cavity radii.
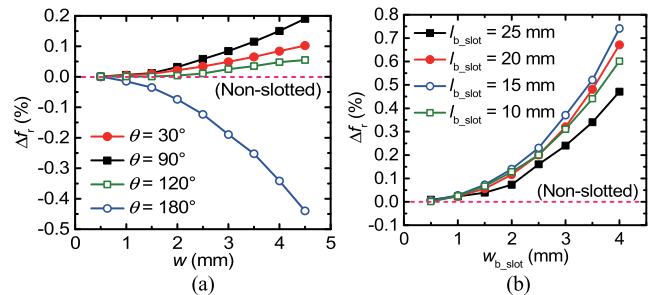

FIGURE 9. The simulated relative resonant frequency shift (Δf_r) of the TM_{101} mode in the slotted hemispherical resonator under different slot dimensions. (a) The top-slotted resonator. (b) The bottom-slotted resonator.

Again, it should be mentioned that the slot dimensions selected for quality-factor quantification are not optimal but are good reference values for the filter design in the next Section. In order to maximize the suppression and Q_u simultaneously, the slot structures can be further optimized in simulation and more slot patterns can be devised flexibly.

III. SLOTTED HEMISPHERICAL RESONATOR BPFS

This Section focuses on RF design of waveguide BPFs based on the proposed slotted hemispherical resonators aiming to further verify the spurious suppression. Several fourth-order filters featuring flexible coupling geometries and slot configurations were devised as proof of concept and their wideband performance was investigated. In order to quantitatively compare RF performance of the filter with previous work, all the filters of this work were designed with following RF specifications—a passband center frequency (f_0) of 10 GHz, a fractional bandwidth (FBW) of 3%, and a passband return loss (RL) of 20 dB. The non-zero denormalized inter-resonator and external coupling coefficients associated with the filter specifications were calculated as $M_{12} = M_{34} = 0.0273$, $M_{23} = 0.0210$, and $M_{S1} = M_{4L} = 0.0311$. Frequency responses of the filters were obtained by performing EM simulation in CST using the coupling-matrix-based filter design methodology in [23].

A. FILTERS A AND B: FLIP-TYPE COUPLED RESONATORS

The first filter prototype (Filter A) of this work is based on the compact flip-type resonator-coupling configuration in [24]
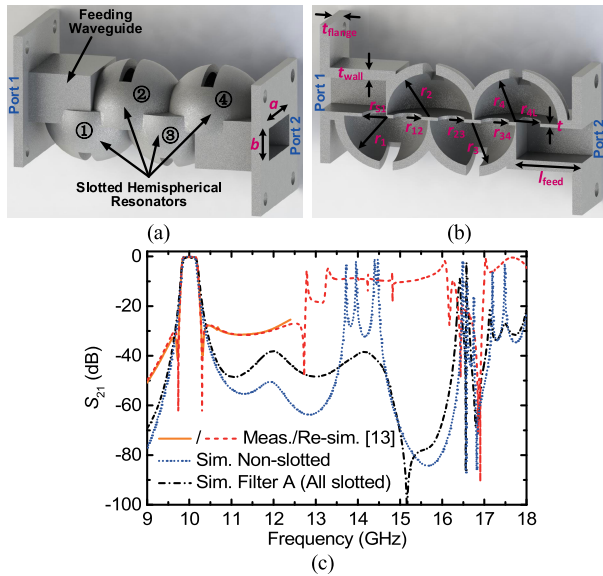
FIGURE 10. The designed *X*-band bottom-fed fourth-order slotted hemispherical resonator BPF: Filter A (With four slotted resonators in a flip-type coupling configuration). (a) The complete fabrication model. (b) The half profile. (c) Comparison in the wideband transmission coefficient (S_{21}).

FIGURE 11. The designed *X*-band bottom-fed fourth-order slotted hemispherical resonator BPF: Filter B (With two slotted and two non-slotted resonators in a flip-type coupling configuration). (a) The complete fabrication model. (b) The half profile. (c) Comparison in the wideband reflection and transmission coefficients (S_{11} and S_{21}).

with feeding waveguides connected to the bottom shells of the first and fourth resonators. The only difference in the geometry is the use of four top-slotted hemispherical resonators. The filter structure is illustrated in Fig. 10(a). The inter-resonator and external couplings of the filter are practically realized by the magnetic coupling through the semicircular and circular apertures, respectively, on the bottom shells of the cavities, as shown in Fig. 10(b). The coupling coefficients are controlled by the radii of these coupling apertures. The EM-simulated wideband power transmission coefficient of the Filter A is plotted in Fig. 10(c) in comparison with previous work. It shows a significant suppression of the spurious resonances at around 14 GHz with a stopband rejection over 38 dB within 10.6–16.3 GHz. The stopband performance has been improved significantly as compared to the results in [13] and [24].

It is inspired from the Filter A that the constituent resonators of the filter can be slotted selectively and the slotted resonators can be assigned flexibly to any resonating node of the filter. Then, we are interested in investigating stopband performance of the filter composed of both non-slotted and slotted resonators and comparing it with the Filter A. Therefore, the second fourth-order filter prototype (Filter B) was designed. Its geometry is illustrated in Fig. 11(a), where the resonators ② and ③ are slotted and the resonators ① and ④ are non-slotted. The only dimensional difference between the two filters is the radii of the resonators ① and ④ [labeled as r_1 and r_4, respectively, in Figs. 10(b) and 11(b), and $r_1 = r_4$]. The simulated frequency responses of the Filters A and B are graphically compared in Fig. 11(c). The result shows that the Filter B has worse suppression of the spurious resonances at
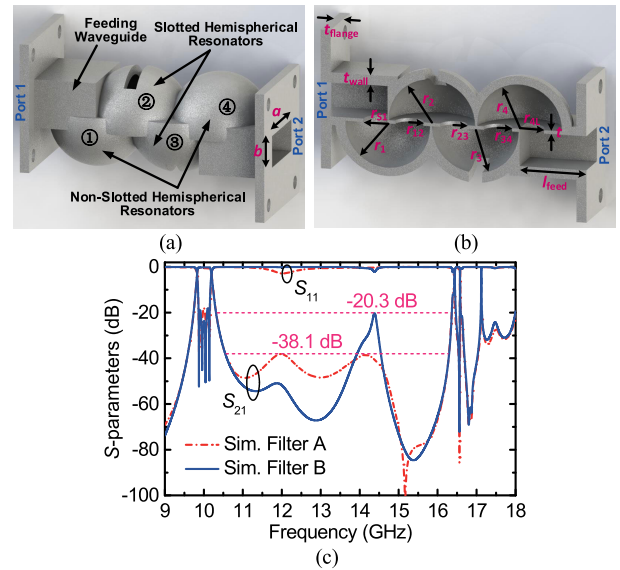
around 14.2 GHz because less number of slotted resonators are used. The corresponding stopband rejection is deteriorated to around 20 dB. The small dimple at ∼12 GHz in the S_{11} parameter of the Filter A should be noticed. Further simulation shows that the dimple is generated by a spurious propagation mode in the resonators ① and ④. This propagation mode is excited as the semicircular apertures for external couplings are significantly large, and it forms a spurious passband at 12 GHz and a stopband at 14 GHz. As the resonators ① and ④ are top-slotted, this propagation mode radiates. Therefore, for the Filter B this dimple is eliminated and no radiation is introduced. Also noteworthy in Fig. 11(c) is the negligible radiation around the suppressed resonances. This is because these resonances are intrinsically detuned and no spurious passband is formed in this region, as shown in Fig. 10(c). As the detuned resonances are suppressed with slots, the introduced radiation can be ignored.

On the other hand, when the resonators ① and ④ are side-fed with waveguides as in Fig. 3(a) and large rectangular apertures are used for strong external couplings, the first spurious passband appears at around 14 GHz because of the TM_{2m1} mode. Under this circumstance if the resonators ① and ④ were top-slotted, significant radiation would be generated.

The simulated RF performance of the Filters A and B indicates a compromise between improving the stopband rejection at the suppressed resonances and mitigating the radiation from the slots. An intuitive solution for the filter to improve stopband rejection is increasing the filter order. However, simply doing this cannot eliminate the radiation. Therefore, we move forward to enhance the stopband
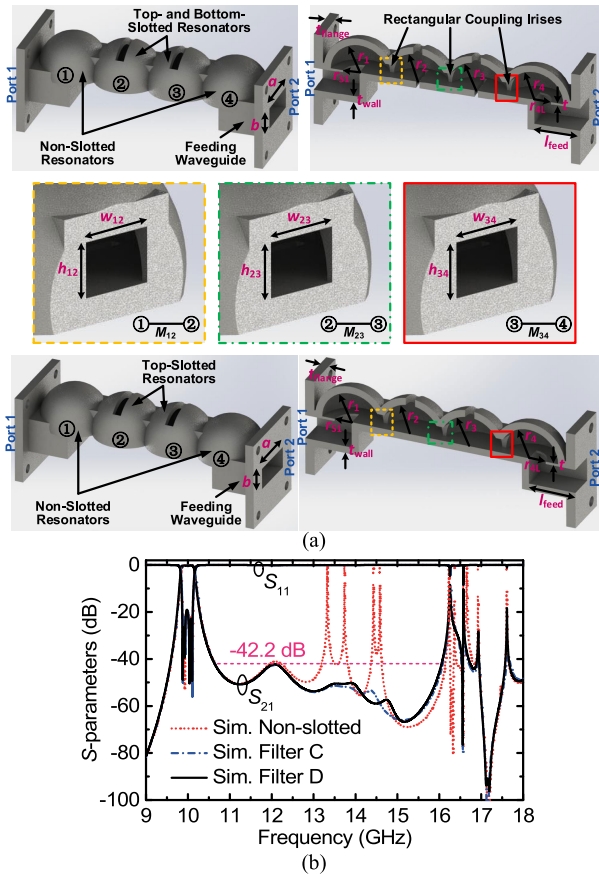
FIGURE 12. The designed *X*-band bottom-fed fourth-order slotted hemispherical resonator BPFs: Filters C and D. (a) Top left: The complete fabrication model of the Filter C; Top right: The half profile of the Filter C; Middle: The inter-resonator coupling apertures; Bottom left: The complete fabrication model of the Filter D; Bottom right: The half profile of the Filter D. (b) Comparison in the wideband reflection and transmission coefficients (S_{11} and S_{21}).

performance by exploring appropriate coupling geometries with slotted resonators selectively assigned to the resonating nodes, without increasing the filter order. In the next part, we present an inline coupling structure for the slotted hemispherical resonators and the other two filter prototypes (Filters C and D) based on this configuration.

B. FILTERS C AND D: IN-LINE COUPLED RESONATORS

The geometries of the Filters C and D are similar and are illustrated in Fig. 12(a). They are composed of two slotted (② and ③) and two non-slotted (① and ④) hemispherical resonators in an inline cascade. The resonators ② and ③ are top- and bottom-slotted for the Filter C, and they are merely top-slotted for the Filter D. The resonators ① and ④ are bottom-fed as for the Filters A and B so that the propagation mode does not radiate. In such a configuration, the inter-resonator coupling is realized by the rectangular aperture between two adjacent resonators. The coupling coefficients are controlled by the widths and heights of the apertures.

EM-simulated wideband power transmission coefficients of the Filters C and D are plotted in Fig. 12(b) in comparison with that of an inline filter composed of non-slotted resonators. The simulated result shows significant suppression of the spurious resonances at around 14 GHz with enhanced stopband rejections over 42 dB. In the simulation, no radiation is found in the stopband because the spurious resonances are detuned before they are suppressed, as indicated in Fig. 12(b). A comparison in the simulated passband responses of the Filters C and D shows little influence of the bottom slots on the IL. The simulated passband ILs of these two filters are only 0.1–0.15 dB higher than that of the non-slotted one. The performance in Figs. 11(c) and 12(b) also indicates deterioration in stopband rejections at around 16.5 GHz due to parasitic resonances induced by the higher order TM_{11} mode in the feeding waveguides. This mode is generated because of the specific external coupling structures. Using other feeding geometries, the parasitic resonances are no longer existent.

Critical design parameters of the aforementioned four filters are summarized in Table 1. The package dimensions such as the cavity and flange thicknesses t_{wall} and t_{flange} were chosen to ensure sufficient mechanical strength of the architectures. The Filters A, C, and D performing relatively good stopband rejections were fabricated for experimental validation purpose. A high-precision metallic 3-D printing technique known as direct metal laser sintering (DMLS) was utilized to deal with the complex and enclosed cavity geometries. This process has been applied to the fabrication of compact and highly-integrated waveguide antenna arrays and their feeding networks [25]–[27] and these components demonstrate excellent RF performance.

IV. FILTER FABRICATION

The filters were 3-D printed with a commercially available aluminum alloy AlSi10Mg [28] supplied in a powder form with a typical particle size of 20–63 μm. The process was carried out in an industrial-grade EOS DMLS printing system [29]. In the software package of the printing system, the electronic model of each filter was properly placed with a tilted posture. The tilted postures of the Filters A and C are graphically exemplified in Fig. 13, and the posture of the Filter D is the same as in Fig. 13(b). Properly tilting the printing model ensured that the structure could be self-supported when the laser-sintered metal powder was stacked layer by layer. In this way, the model could be 3-D printed as a single part without generating any metallic support inside the cavities. This is important as the internal metallic support could be hardly removed and would disable the device. Under such postures, the metallic support, as illustrated in Fig. 13, was only generated outside the cavities. The sintering was performed using a 400-W yttrium fiber laser and a vertical printing resolution of 60 μm was used. After the sintering was done, the external metallic support was removed manually from the as-printed workpiece. Then, the workpiece was polished and sandblasted to reduce the surface roughness.

TABLE 1. Critical dimensions of the designed fourth-order slotted hemispherical resonator waveguide filters.

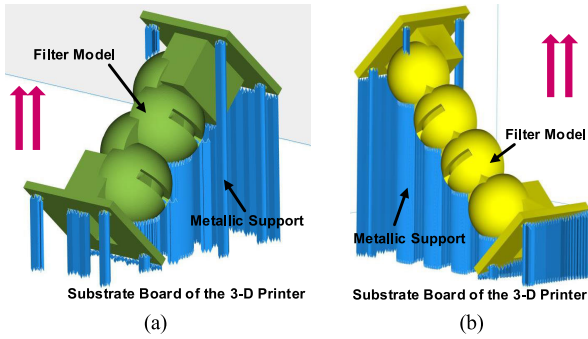| Filters	$r_1 (= r_4)$ (mm)	$r_2 (= r_3)$ (mm)	$w_{12} (= w_{34})$ (mm)	$h_{12} (= h_{23} = h_{34})$ (mm)	w_{23} (mm)	$r_{12} (= r_{34})$ (mm)	r_{23} (mm)	$r_{S1} (= r_{4L})$ (mm)	θ (°)	w (mm)	l_{b_slot} (mm)	w_{b_slot} (mm)	t_{flange} (mm)	l_{feed} (mm)	t_{wall} (mm)	t (mm)
A	12.691	12.981	—	—	—	4.241	3.977	7.297	90	4	—	—	3	20	3	1
B	12.675	12.981	—	—	—	4.241	3.977	7.297	90	4	—	—	3	20	3	1
C	12.599	12.749	9.209	6	8.498	—	—	7.255	90	4	23	1.5	4	20	3	1
D	12.620	12.750	9.209	6	8.498	—	—	7.255	90	4	0	0	4	20	3	1

FIGURE 13. Illustrations of the exemplified tilted postures of the filter models for 3-D printing. The red dual-arrow symbols indicate the vertical printing orientation. (a) The Filter A. (b) The Filter C.

FIGURE 14. The metallic 3-D printed Filter A. (a) The EM-simulated and RF-measured passband reflection and transmission coefficients. The dotted lines represent the re-simulated performance of the filter taking into account the volume shrinkage. The inset shows the S_{21} group delay response. (b) The EM-simulated and RF-measured wideband reflection and transmission coefficients. The inset is a photograph of the fabricated Filter A.

V. MEASUREMENT AND CHARACTERIZATION

A. TRANSMISSION AND REFLECTION RESPONSES

The transmission and reflection responses of the 3-D printed filters were measured by using a Keysight N5247A network analyzer [30] under a two-port waveguide thru-reflect-line calibration. The frequency responses at *X* and *Ku* bands were measured individually. For the measurement of the *Ku*-band response, a pair of *X*-to-*Ku*-band waveguide tapers were used and the network analyzer was calibrated at *Ku* band. EM-simulated and RF-measured frequency responses and photographs of the fabricated filters are graphically presented in Figs. 14–16, showing good agreement. Note that all the measured passbands exhibit a frequency shift (Δf) around 0.9% toward higher frequencies. The Δf is attributed to the volume shrinkage of the metallic printed cavities. The shrinkage was induced in the laser sintering process by the phase transformation and the contraction of solids from the solidification temperature to ambient temperature [31]–[33]. This phenomenon is caused by intrinsic property of the printing material and is hardly controllable in the process of 3-D printing. Because of the shrunk cavities, the resonant frequency of each resonator is increased and the inter-resonator as well as external couplings are decreased. This deteriorates passband return loss and decreases bandwidth of the filter. The shrinkage also occurs in other 3-D printing techniques such as stereolithography apparatus (SLA) [34], where it is induced by phase transformation of photosensitive resins from liquid to solid. The shrinkage appears to be more significant for metallic 3-D printed parts because high temperature is involved in the process.
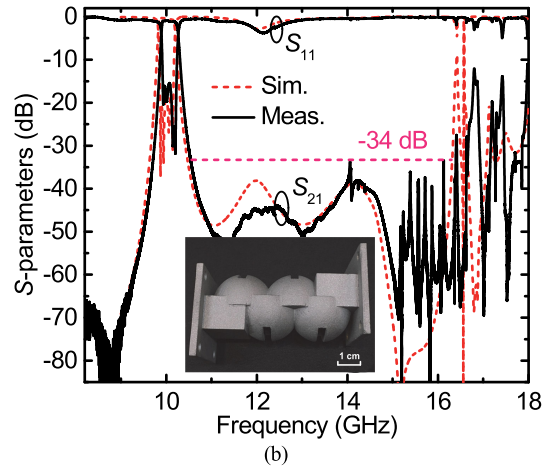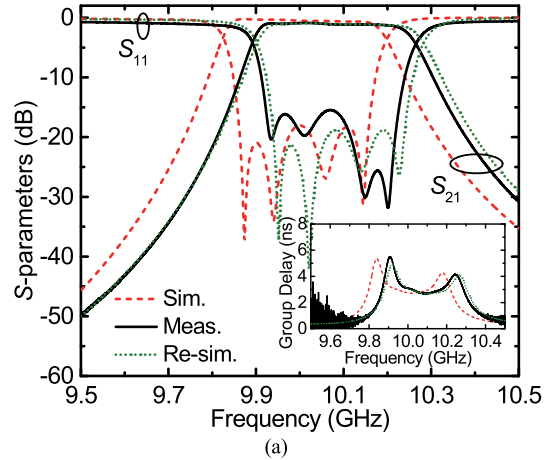
As shown in Figs. 14(a), 15(a), and 16(a), the measured passband RLs of the filters are greater than 15 dB, where the RL is over 20 dB for the Filter C. The good passband performance demonstrates high fabrication accuracy of the employed DMLS process. The measured passband S_{21} group delays of the filters are less than 6 ns.

The tolerance introduced by the volume shrinkage was evaluated by performing EM simulation through slightly reducing size of the filters' cavities. The re-simulation aimed to obtain passband responses in better agreement
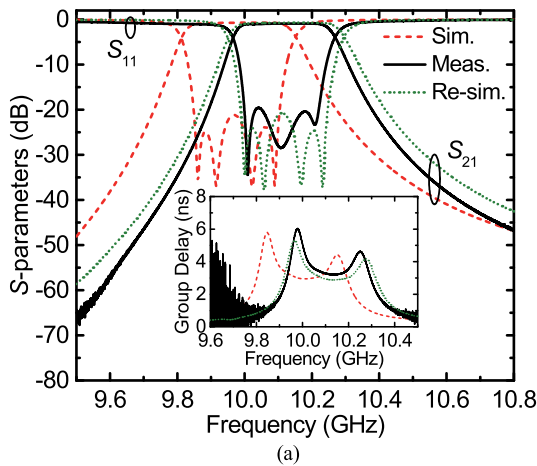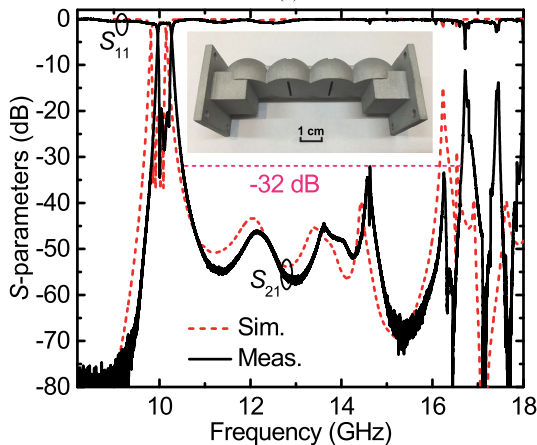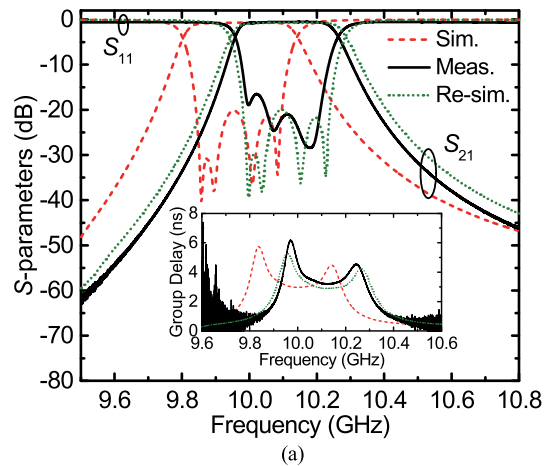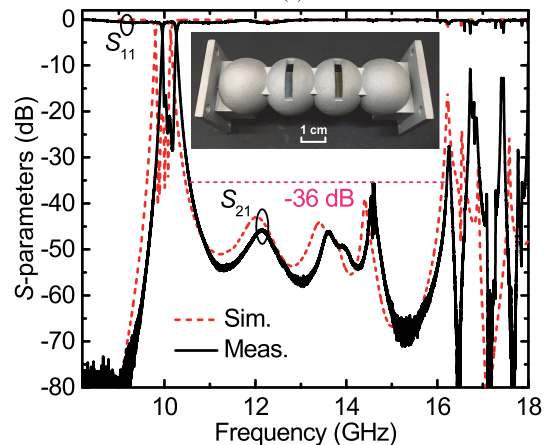
FIGURE 15. The metallic 3-D printed Filter C. (a) The EM-simulated and RF-measured passband reflection and transmission coefficients. The dotted lines represent the re-simulated performance of the filter taking into account the volume shrinkage. The inset shows the S_{21} group delay response. (b) The EM-simulated and RF-measured wideband reflection and transmission coefficients. The inset is a photograph of the fabricated Filter C.

FIGURE 16. The metallic 3-D printed Filter D. (a) The EM-simulated and RF-measured passband reflection and transmission coefficients. The dotted lines represent the re-simulated performance of the filter taking into account the volume shrinkage. The inset shows the S_{21} group delay response. (b) The EM-simulated and RF-measured wideband reflection and transmission coefficients. The inset is a photograph of the fabricated Filter D.

with the measured ones. To simplify the analysis, the re-simulation was first done in CST by uniformly scaling the entire simulation model of each demonstrated filter, making the filter model slightly smaller than the optimal. Then, we ran the simulation and adjusted the scaling factor, obtaining the re-simulated passbands that shifted towards higher frequencies and were in better agreement with the measured ones in term of center frequency. The re-simulated passband responses of the filters are included in Figs. 14(a), 15(a), and 16(a) for comparison. Next, we measured the dimensions in the scaled filter models and compared them with the originals. The critical dimensions after scaling are smaller than the originals in a range of 0.02–0.33 mm. In particular, the scaled radii of the air-filled hemispherical cavities are about 0.13 mm smaller for the Filter A, and about 0.18 mm smaller for the Filters C and D.

Note that this is only a simple estimation of the tolerance values. However, it provides good reference values to further optimize the filter design and the process recipe

of 3-D printing. Quantifying the tolerance accurately only by simulation is complicated because the practical shrinkage is not uniform and is dependent on many other aspects such as geometrical characteristics of the cavities. The most accurate method to quantify the tolerance and its influence on RF performance of the filters is using X-ray microcomputed tomography (micro-CT) to reconstruct 3-D electronic models from the 3-D printed filters. The practical dimensions of the filters can be measured directly from the CT-rebuilt 3-D models and the models can be used directly to characterize the RF performance through re-simulation.

An effective approach to minimize the impact of volume shrinkage is performing a structural compensation [35]. In particular, for cavity resonators and filters, this can be done before the 3-D printing process by properly increasing the volume of the air-filled cavity in the electronic model according to the quantified tolerance values.

The measured wideband performance in Figs. 14(b), 15(b), and 16(b) shows broad spurious-free stopbands of the filters, verifying suppression of the spurious resonances. The
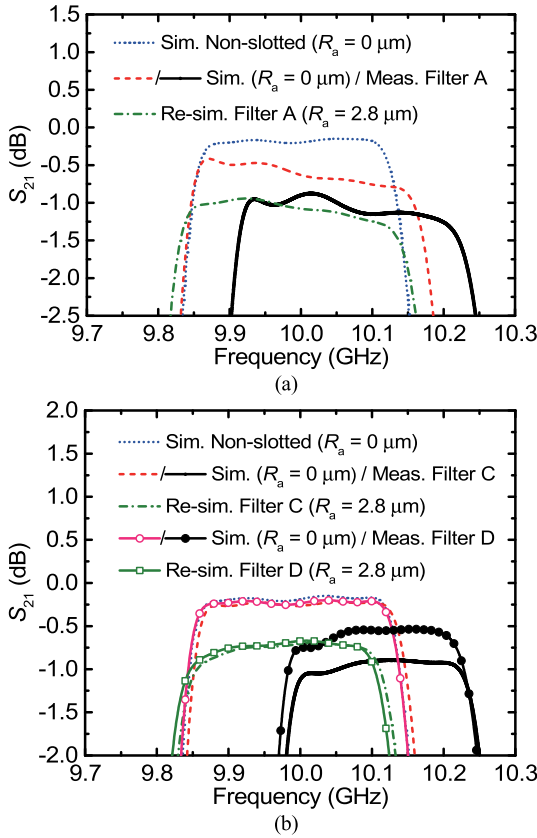
FIGURE 18. Measured surface profiles of the 3-D printed aluminum alloy in the waveguide flange regions of the filters. The profiles 1–3 were measured from the Filters A, C, and D, respectively.

FIGURE 17. EM-simulated and RF-measured passband transmission coefficients of the filters. In the simulation, pure aluminum was used for the cavity boundaries and different surface roughness values were taken into consideration. (a) The flip-type coupling geometry. (b) The inline coupling geometry.

spurious-free regions have been extended to beyond 18 GHz with stopband rejections better than 32 dB in a range up to 16.2 GHz. The stopband rejection in this range could be further improved to approach the simulated value (>40 dB) if the shrinkage-induced tolerance were minimized. In the measured range, the worst stopband rejections are deteriorated to 11–12 dB beyond 16.8 GHz.

A close-up view for the filters' passband transmission coefficients are shown in Fig. 17. The measured average passband ILs for the Filters A, C, and D are 1.1, 0.6, and 0.9 dB, respectively, and they are higher than the corresponding simulated values. The increased IL is mainly attributed to the lowered electrical conductivity of the printed metal. First, surface roughness of the metallic cavities was not taken into account in the simulation. Secondly, the effective electrical conductivity of the practical aluminum alloy is intrinsically lower than that of pure aluminum used in the simulation. To quantify influence of the surface roughness on the passband IL, the surface profiles in several relatively smooth regions of the metallic printed waveguide flanges of the filters were measured by using a Bruker DektakXT stylus profiler [36] based on contact profilometry. A linear scanning range of 1 mm was used under a sampling resolution
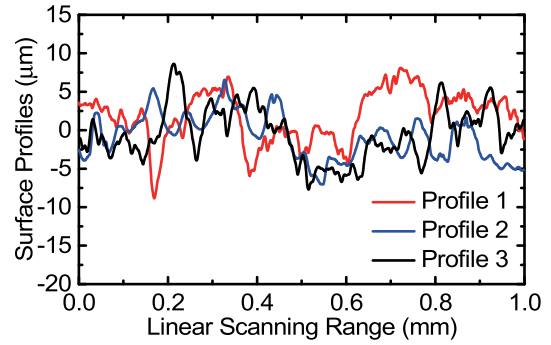
of 0.333 μm. The measured profiles are depicted in Fig. 18. The average surface roughness (R_a) and root mean square surface roughness (R_q) were measured directly in the profiler. A group of measured typical R_a and R_q values are 2.775 and 3.429 μm, respectively. Taking into account the R_a value of 2.8 μm, the re-simulated passband S_{21} parameters are obtained and plotted in Fig. 17 for comparison. As can be seen, under circumstance of pure aluminum (with an electrical conductivity of 3.56×10^7 S/m) cavity boundaries, this roughness contributes to an increase of about 0.5–0.7 dB in the passband IL. The corresponding practical Q_cs of the top-slotted and bottom-slotted hemispherical resonators are estimated to be 1520. Several measures can be taken to reduce the IL through improving the effective electrical conductivity of the metal. For example, abrasive flow machining process can be applied to polish the printed metal and further minimize the internal surface roughness [37]. Then, a thick layer of copper can be electroplated to perform as the primary conductive layer [38]. Finally, a passivation layer of silver or gold can be plated to prevent oxidation of copper [9], [18], [19]. It should be noticed that the surface profiles in Fig. 18 were sampled in limited regions of the printed metal and they cannot precisely represent the morphology for the other surface areas. For example, the roughness inside the cavity could be larger because the internal surface could not be polished as well as the outside. However, the measured roughness values are still good references to evaluate the loss of the filter because the re-simulated S_{21} parameters are close to the measured ones.

Fig. 19 shows the calculated loss $(1 - |S_{11}|^2 - |S_{21}|^2)$ of the demonstrated filters. This loss includes the conductor loss from the metal and the radiation loss from the slots. It can be seen that in the passbands this loss is in the range of 0.5–1.2 dB mainly due to the conductor loss. On the other hand, at several stopband frequencies this loss is significantly larger (e.g., >4 dB) because of the enhanced radiation. It is possible to mitigate impact of the stop radiation on external circuits by attaching microwave absorbers onto the slots, and further measured RF performance of the filters with the absorbers [39] attached shows no significant difference to the results in Figs. 14–16.
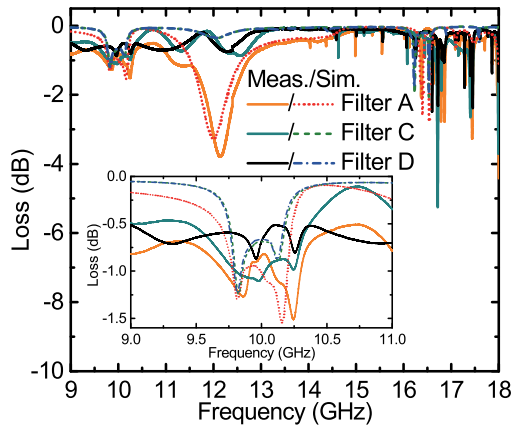
FIGURE 19. The loss $(1 - |S_{11}|^2 - |S_{21}|^2)$ of the demonstrated filters.
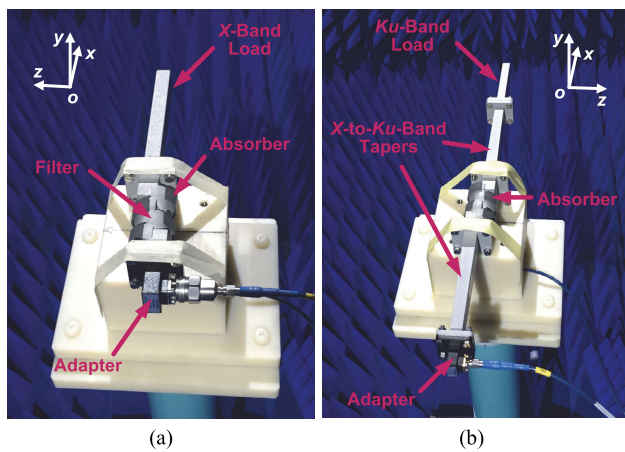

FIGURE 20. Photographs of the setup in the anechoic chamber for measuring far-field radiation patterns of the filter A. (a) At the passband center frequency (measurement at *X* band). (b) At the stopband frequencies (measurement at *Ku* band).
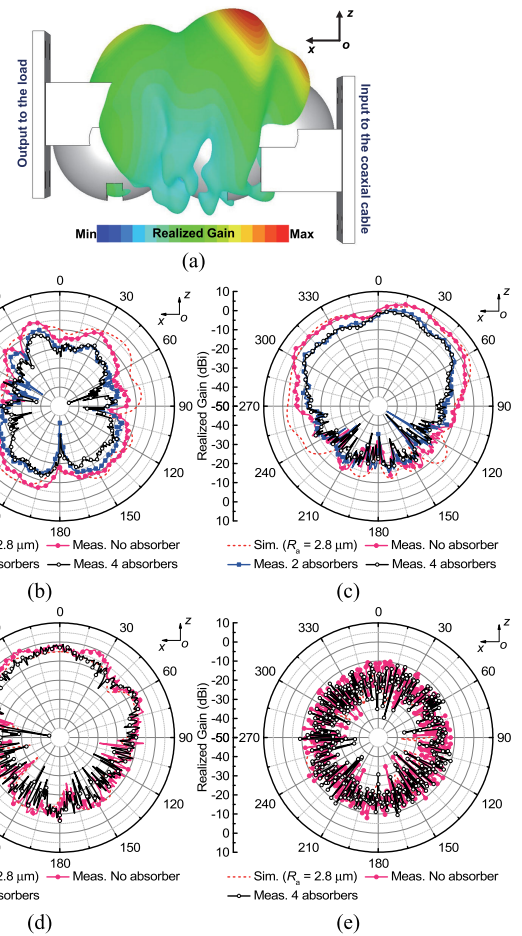

FIGURE 21. EM-simulated and RF-measured far-field radiation patterns of the Filter A. (a) The simulated 3-D realized gain pattern at 12 GHz showing the orientation with a peak gain of 5.27 dBi. (b) At 10.1 GHz. (c) At 12.14 GHz. (d) At 14.2 GHz. (e) At 16.5 GHz.

B. RADIATION PERFORMANCE

To rigorously evaluate radiation performance of the slotted cavities, the far-field radiation patterns at the passband center frequencies and several stopband frequencies at *Ku* band with the maximum loss $(1 - |S_{11}|^2 - |S_{21}|^2)$ of the filters were measured in an anechoic chamber. This was done at *X* and *Ku* bands individually. In the measurement, the input waveguide port of the tested filter was mated to a coaxial cable of the chamber system and the output waveguide port was matched to minimize the power reflection. This allows the tested filter to work normally with the measured frequency response. For the far-field measurement at *X* band, the input port was transitioned to the coaxial cable through a WR-90-waveguide-to-coax adapter and the output port was connected to an *X*-band waveguide matching load. For the far-field measurement at *Ku* band, the input port was transitioned to the cable through an *X*-to-*Ku*-band waveguide taper in-series cascaded to a WR-62-waveguide-to-coax adapter, and the output port was connected to a *Ku*-band waveguide matching load through the other *X*-to-*Ku*-band taper. The radiation

patterns before and after the absorbers were attached to the slots were measured. An exemplified measurement setup for the filter A is shown in Fig. 20. To acquire the patterns showing the strongest radiation, all the tested filters were laid down horizontally in the *xoz*-plane (see Fig. 20), because in this orientation the filters have the maximum simulated realized gains. A simulated realized gain pattern of the Filter A in the *xoz*-plane is illustrated in Fig. 21(a).

The EM-simulated and RF-measured far-field radiation patterns of the filters are graphically compared in Figs. 21–23, showing good agreement. At the passband center frequency of 10.1 GHz, the measured realized gains are mostly lower than −10 dBi. When all slots of the filters are covered with the absorbers, the measured peak realized gains are lower than −10, −18, and −18 dBi, respectively, for the Filters A, C, and D. This verifies little radiation in the passbands. For the Filter A, the measured peak gain at the stopband frequency of 12.14 GHz is 5.187 dBi that is close to the simulated value of 5.27 dBi. After slots on the resonators ① and ④ are covered with the absorbers, the measured peak gain is reduced to 1.451 dBi. The 1-mm thick
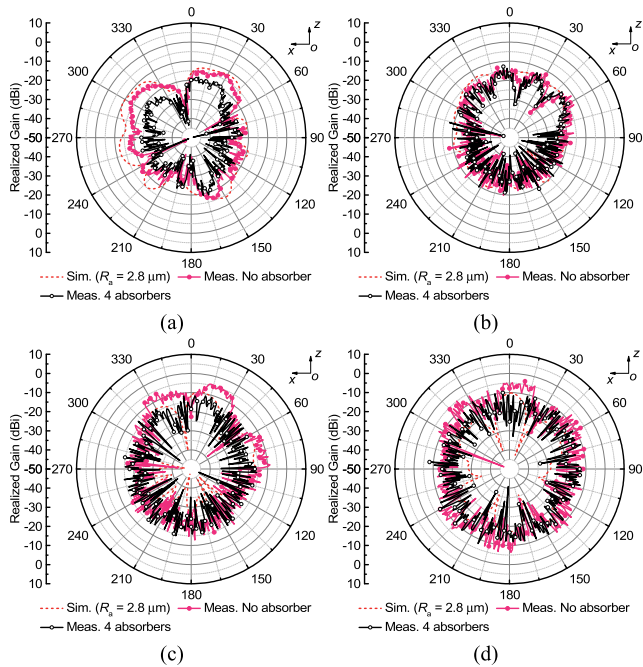
FIGURE 22. EM-simulated and RF-measured far-field radiation patterns of the Filter C. (a) At 10.1 GHz. (b) At 12.58 GHz. (c) At 14.6 GHz. (b) At 16.72 GHz.
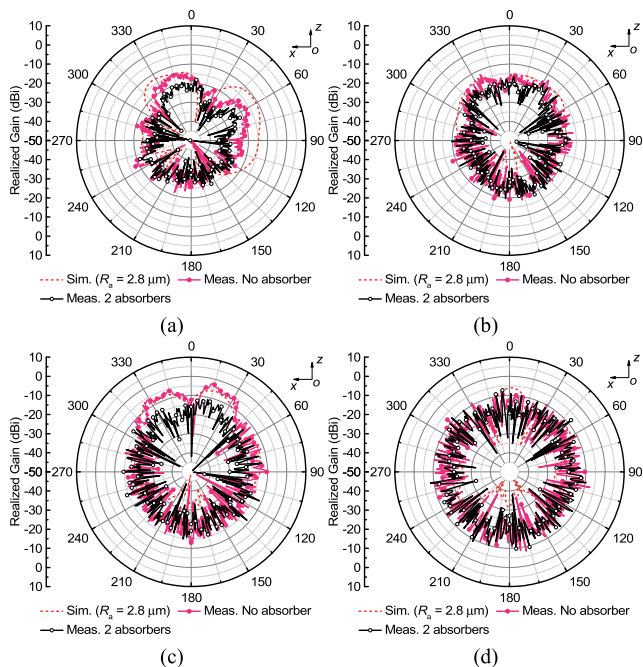

FIGURE 23. EM-simulated and RF-measured far-field radiation patterns of the Filter D. (a) At 10.1 GHz. (b) At 12.3 GHz. (c) At 14.6 GHz. (d) At 16.72 GHz.

absorbers provide an attenuation of about 4 dB (an attenuation rate of ∼40 dB/cm at 12 GHz [39]). After all the slots are covered with the absorbers, the measured peak gain is further decreased to −0.015 dB. As can be seen in Fig. 21(c), the patterns in cases of the slots all covered and partially
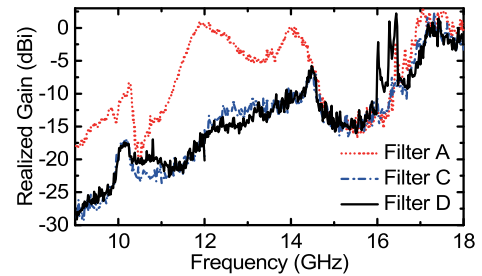

FIGURE 24. Measured peak realized gains for the filters with all slots covered with the absorbers.
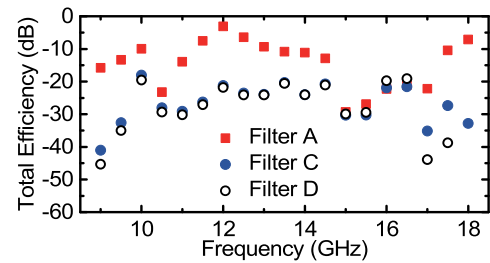

FIGURE 25. Simulated total efficiencies of radiation for the filters.

covered with the absorbers are very similar, verifying the discussion in Section III A that the radiation at around 12 GHz mainly comes from the slotted resonators ① and ④. For the Filters C and D with the non-slotted resonators ① and ④, the measured peak gains are as low as −15 dBi at 12.58 and 12.3 GHz, respectively. At the other selected stopband frequencies, the measured realized gains of the filters with absorbers attached to the slots are smaller than −10 dBi.

The measured peak realized gains and simulated total efficiencies of radiation with relation to frequencies from 9 to 18 GHz are plotted in Figs. 24 and 25, respectively. The practical total efficiencies were not obtained due to limitation of the measurement facility. In this frequency range, the peak realized gains of the Filters C and D are mostly lower than −10 dBi, and the corresponding total efficiencies are smaller than −20 dB. The result shows stopband radiation of these filters much weaker than that of the Filter A. The peak realized gains of the Filters C and D are increased at the higher stopband edge, but the total efficiencies are still low, showing very small leakage of the input power from the slots.

A quantitative comparison in major specifications of the demonstrated filters with previous work is summarized in Table 2. The cavity-slotted filters of this work are superior in much wider spurious-free stopbands over the results in [11] and [13]–[15], and a spurious-free frequency ratio of >1.8:1 with stopband rejections over 36 dB has been achieved. The stopband rejections of the waveguide filters in [16] and [17] are even higher, but they are more dependent on the FBW and order of the filters. In spite of imperfection in the filter performance in terms of relatively large ILs and Δf s, these prototypes successfully demonstrate the method

TABLE 2. Comparison with previously reported 3-D printed waveguide BPFs.

References	f_0 (GHz)	FBW (%)	Filter Order	RL (dB)	IL (dB)	Δf (%)	f_1/f_0	[a]Spurious Suppression?	Monolithic Printing?	Types of Resonators	Fabrication Techniques
[11]	10	5	5	>20	0.11	0.05	1.32:1	—	—	S	SLA+EP Cu
[12]	34.8	5.7	4	>12	1.7−3.1	0.57	N/A	—	Yes	S	SLA+ELP Cu
[13]	10	3	4	>18	0.24	<0.01	1.27:1	—	Yes	SS	SLA+EP Cu
[14], [15]	32	1/3/5	2/4	>10−17	0.43−0.9	<0.47	1.37:1	—	Yes	H	SLA+ELP Cu/Ag
[16]	12.875	1.9	9	>20	0.55−0.8	0.12	1.55:1	Yes (>55 dB)	Yes	SE	SLM
[17]	12.875/14.125	1.94/1.77	3/5	>18	0.2	<0.2	>1.7:1	Yes (>55 dB)	Yes	SE	SLM
[18]	32.2	13.6	5	>17	0.23−0.5	0.37	N/A	—	Yes	SR	SLA+EP Cu/ELP Ag
[19]	87.5	11.5	5	>18	0.3−0.5	2.78	N/A	—	Yes	SR	SLA+EP Cu/Au
[20]	8.23	5.23	8	>10	0.32−0.68	0.16	N/A	—	Yes	SC	SLA+ELP Cu/Ag
T.W. Filter A	10.09	3	4	>15	1.1	0.9	>1.8:1	Yes (>34 dB)	Yes	SH	DMLS
T.W. Filter C	10.1	3	4	>20	0.6	1	>1.8:1	Yes (>32 dB)	Yes	SH	DMLS
T.W. Filter D	10.1	3	4	>16	0.9	1	>1.8:1	Yes (>36 dB)	Yes	SH	DMLS

[*]T.W.: This work; f_1/f_0: The frequency ratio of the measured first spurious passband to the fundamental-mode passband; EP: Electroplating; ELP: Electroless plating; N/A: Not available; Types of resonators: spherical (S), slotted spherical (SS), hemispherical (H), super-ellipsoid (SE), slotted rectangular (SR), slotted circular (SC), and slotted hemispherical (SH).

[a]The stopband rejection is more dependent on the FBW and the filter order.

of slotting cavity resonators for purpose of spurious suppression. In this work, the slots are functional geometries and are in significant contrast to the ones in [13] and [18]–[20].

Finally, it should be mentioned that the limited number of the demonstrated filters does not degrade the novelty of this work. First, the proposed method to suppress spurious resonances with slots can be applied to other types of cavity resonators. Secondly, it can be extrapolated to design even higher order filters with enhanced structural flexibility. In addition, the presented filter structures can be implemented by other polymer-based AM techniques such as SLA [40] and digital light processing [41] with incorporation of copper electroplating or electroless copper/silver plating process. The polymer-based and copper-coated filters can have even lighter weight due to a lower density of the polymer, and furthermore much less conductor loss because of a smaller surface roughness and a higher electrical conductivity of the conductive layer.

VI. CONCLUSION

This work provides a method to effectively suppress unwanted spurious modes in air-filled metallic hemispherical cavity resonators to extend spurious-free stopbands of the BPFs. A study focusing RF design, monolithic 3-D printing, and characterization of slotted hemispherical resonator waveguide BPFs has been presented systematically. The spurious suppression is achieved by interrupting surface current of the spurious modes of the resonator with slots, and significantly enhanced stopband performance of the filters has been experimentally validated. The high-quality metallic DMLS process allows the complex filter geometries of this work to be fabricated precisely. The filters demonstrate good passband performance—average IL: 0.6–1.1 dB, RL: >20 dB, and Δf: 0.9%–1%, and a spurious-free frequency ratio of

>1.8:1 with stopband rejections over 36 dB. Furthermore, the radiation performance of the slotted filters has been quantified, showing that the passband radiation is negligible and the stopband radiation can be minimized by carefully designing the coupling geometries, selectively assigning slotted cavities to the resonant nodes, and covering slots with microwave absorbers. The principle of slotting is also applicable to other types of cavity resonators to enhance stopband performance of the BPFs.

REFERENCES

[1] R. V. Snyder, A. Mortazawi, I. Hunter, S. Bastioli, G. Macchiarella, and K. Wu, "Present and future trends in filters and multiplexers," *IEEE Trans. Microw. Theory Techn.*, vol. 63, no. 10, pp. 3324–3360, Oct. 2015.

[2] S. Amari, "Application of representation theory to dual-mode microwave bandpass filters," *IEEE Trans. Microw. Theory Techn.*, vol. 57, no. 2, pp. 430–441, Feb. 2009.

[3] H. Hu, K. L. Wu, and R. J. Cameron, "Stepped circular waveguide dual-mode filters for broadband contiguous multiplexers," *IEEE Trans. Microw. Theory Techn.*, vol. 61, no. 1, pp. 139–145, Jan. 2013.

[4] L. Accatino, G. Bertin, and M. Mongiardo, "A four-pole dual mode elliptic filter realized in circular cavity without screws," *IEEE Trans. Microw. Theory Techn.*, vol. 44, no. 12, pp. 2680–2687, Dec. 1996.

[5] S.-L. Lai and W.-G. Lin, "A five mode single spherical cavity microwave filter," in *IEEE MTT-S Int. Microw. Symp. Dig.*, Albuquerque, NM, USA, vol. 2, Jun. 1992, pp. 909–912.

[6] F. Calignano, D. Manfredi, E. P. Ambrosio, S. Biamino, M. Lombardi, E. Atzeni, A. Salmi, P. Minetola, L. Iuliano, and P. Fino, "Overview on additive manufacturing technologies," *Proc. IEEE*, vol. 105, no. 4, pp. 593–612, Apr. 2017.

[7] H. Xin and M. Liang, "3-D-printed microwave and THz devices using polymer jetting techniques," *Proc. IEEE*, vol. 105, no. 4, pp. 737–755, Apr. 2017.

[8] T.-H. Chio, G.-L. Huang, and S.-G. Zhou, "Application of direct metal laser sintering to waveguide-based passive microwave components, antennas, and antenna arrays," *Proc. IEEE*, vol. 105, no. 4, pp. 632–644, Apr. 2017.

[9] A. I. Dimitriadis, T. Debogovic, M. Favre, M. Billod, L. Barloggio, J.-P. Ansermet, and E. de Rijk, "Polymer-based additive manufacturing of high-performance waveguide and antenna components," *Proc. IEEE*, vol. 105, no. 4, pp. 668–676, Apr. 2017.

[10] W. J. Otter and S. Lucyszyn, "Hybrid 3-D-printing technology for tunable THz applications," *Proc. IEEE*, vol. 105, no. 4, pp. 756–767, Apr. 2017.

[11] C. Guo, X. Shang, M. J. Lancaster, and J. Xu, "A 3-D printed lightweight X-band waveguide filter based on spherical resonators," *IEEE Microw. Wireless Compon. Lett.*, vol. 25, no. 7, pp. 442–444, Jul. 2015.

[12] Y. Li, J. Li, M. Zhang, H. Wang, J. Xu, and S. Xiao, "A monolithic stereolithography 3-D printed *Ka*-band spherical resonator bandpass filter," in *IEEE Radio Wireless Symp. Dig.*, Anaheim, CA, USA, Jan. 2018, pp. 56–59.

[13] C. Guo, X. Shang, J. Li, F. Zhang, M. J. Lancaster, and J. Xu, "A lightweight 3-D printed *X*-band bandpass filter based on spherical dual-mode resonators," *IEEE Microw. Wireless Compon. Lett.*, vol. 26, no. 8, pp. 568–570, Aug. 2016.

[14] J. Li, C. Guo, L. Mao, and J. Xu, "Compact high-*Q* hemispherical resonators for 3-D printed bandpass filter applications," in *IEEE MTT-S Int. Microw. Symp. Dig.*, Honolulu, HI, USA, Jun. 2017, pp. 1591–1594.

[15] J. Li, C. Guo, L. Mao, J. Xiang, G.-L. Huang, and T. Yuan, "Monolithically 3-D printed hemispherical resonator waveguide filters with improved out-of-band rejections," *IEEE Access*, vol. 6, pp. 57030–57048, 2018.

[16] P. A. Booth and E. V. Lluch, "Realising advanced waveguide bandpass filters using additive manufacturing," *IET Microw., Antennas Propag.*, vol. 11, no. 14, pp. 1943–1948, Nov. 2017.

[17] P. A. Booth and E. V. Lluch, "Enhancing the performance of waveguide filters using additive manufacturing," *Proc. IEEE*, vol. 105, no. 4, pp. 613–619, Apr. 2017.

[18] J. Li, C. Guo, L. Mao, and J. Xu, "Lightweight low-cost *Ka*-band 3-D printed slotted rectangular waveguide bandpass filters," in *Proc. IEEE Int. Symp. Antennas Propag.*, San Diego, CA, USA, Jul. 2017, pp. 2647–2648.

[19] X. Shang, P. Penchev, C. Guo, M. J. Lancaster, S. Dimov, Y. Dong, M. Favre, M. Billod, and E. de Rijk, "*W*-band waveguide filters fabricated by laser micromachining and 3-D printing," *IEEE Trans. Microw. Theory Techn.*, vol. 64, no. 8, pp. 2572–2580, Aug. 2016.

[20] C. Guo, J. Li, J. Xu, and H. Li, "An *X*-band lightweight 3-D printed slotted circular waveguide dual-mode bandpass filter," in *Proc. IEEE Int. Symp. Antennas Propag.*, San Diego, CA, USA, Jul. 2017, pp. 2645–2646.

[21] K. Zhang and D. Li, *Electromagnetic Theory for Microwaves and Optoelectronics*, 2nd ed. Berlin, Germany: Springer-Verlag, 2008.

[22] (May 2018). *CST Computer Simulation Technology*. Arroyo Grande, CA, USA. [Online]. Available: https://www.cst.com.

[23] J. S. Hong and M. J. Lancaster, *Microstrip Filters for RF/Microwave Applications*. New York, NY, USA: Wiley, 2001.

[24] J. Li, C. Guo, L. Mao, and J. Xu, "3D printed bandpass filters using compact high-*Q* hemispherical resonators with improved out-of-band rejection," *Electron. Lett.*, vol. 53, no. 6, pp. 413–415, Mar. 2017.

[25] G.-L. Huang, S.-G. Zhou, and T. Yuan, "Design of a compact wideband feed cluster with dual-polarized sum- and difference-patterns implemented via 3-D metal printing," *IEEE Trans. Ind. Electron.*, vol. 65, no. 9, pp. 7353–7362, Sep. 2018.

[26] G.-L. Huang, C.-Z. Han, W. Xu, T. Yuan, and X. Zhang, "A compact 16-way high-power combiner implemented via 3-D metal printing technique for advanced radio-frequency electronics system applications," *IEEE Trans. Ind. Electron.*, vol. 66, no. 6, pp. 4767–4776, Jun. 2019.

[27] G.-L. Huang, S.-G. Zhou, C.-Y.-D. Sim, T.-H. Chio, and T. Yuan, "Lightweight perforated waveguide structure realized by 3-D printing for RF applications," *IEEE Trans. Antennas Propag.*, vol. 65, no. 8, pp. 3897–3904, Aug. 2017.

[28] EOS. (Jul. 2018). *Aluminium AlSi10Mg Material Data Sheet*. [Online]. Available: https://www.eos.info

[29] EOS (Jul. 2018). *Electro Optical Systems GmbH Company*, [Online]. Available: https://www.eos.info

[30] (Oct. 2018). *Keysight Technologies*. [Online]. Available: https://www.keysight.com

[31] S. Singh, V. S. Sharma, and A. Sachdeva, "Optimization and analysis of shrinkage in selective laser sintered polyamide parts," *Mater. Manuf. Processes*, vol. 27, no. 6, pp. 707–714, 2012.

[32] J. G. Zhou and Z. He, "Rapid pattern based powder sintering technique and related shrinkage control," *Mater. Des.*, vol. 19, nos. 5–6, pp. 241–248, Dec. 1998.

[33] H. H. Zhu, L. Lu, and J. Y. H. Fuh, "Study on shrinkage behaviour of direct laser sintering metallic powder," *Proc. Inst. Mech. Eng., B, J. Eng. Manuf.*, vol. 220, no. 2, pp. 183–190, 2006.

[34] W. L. Wang, C. M. Cheah, J. Y. H. Fuh, and L. Lu, "Influence of process parameters on stereolithography part shrinkage," *Mater. Des.*, vol. 17, no. 4, pp. 205–213, 1996.

[35] Q. Huang, J. Zhang, A. Sabbaghi, and T. Dasgupta, "Optimal offline compensation of shape shrinkage for three-dimensional printing processes," *IIE Trans.*, vol. 47, no. 5, pp. 431–441, 2015.

[36] Bruker. (Nov. 2018). *DektakXT Stylus Profilers*. [Online]. Available: https://www.bruker.com

[37] S. Zhang, W. Liu, L. Yang, C. Zhu, C. Li, J. Li, and X. Li, "Study on abrasive flow ultra-precision polishing technology of small hole," in *Int. Conf. Mechatron. Autom.*, Changchun, China, Aug. 2009, pp. 4305–4309.

[38] M. Salek, X. Shang, R. C. Roberts, M. J. Lancaster, F. Boettcher, D. Weber, and T. Starke, "W-band waveguide bandpass filters fabricated by micro laser sintering," *IEEE Trans. Circuits Syst. II, Express Briefs*, vol. 66, no. 1, pp. 61–65, Jan. 2019.

[39] Laird Technologies. (Mar. 2019). *Eccosorb GDS Microwave Absorber*. [Online]. Available: https://www.lairdtech.com

[40] G. P. Le Sage, "3D printed waveguide slot array antennas," *IEEE Access*, vol. 4, pp. 1258–1265, 2016.

[41] J. Shen and D. S. Ricketts, "Additive manufacturing of complex millimeter-wave waveguides structures using digital light processing," *IEEE Trans. Microw. Theory Techn.*, vol. 67, no. 3, pp. 883–895, Mar. 2019.

JIN LI (S'11–M'17) received the B.E. degree in electronic information engineering and the Ph.D. degree in radio physics from the University of Electronic Science and Technology of China, Chengdu, Sichuan, China, in 2010 and 2017, respectively.

From 2013 to 2015, he was a Visiting Research Scholar with the Birck Nanotechnology Center, School of Electrical and Computer Engineering, Purdue University, West Lafayette, IN, USA, supported by the China Scholarship Council under the State Scholarship Fund. He was an External Research Specialist with the ATR National Key Laboratory of Defense Technology, Shenzhen University, Shenzhen, Guangdong, China, from 2017 to 2018, where he is currently a Postdoctoral Research Fellow with the College of Electronics and Information Engineering. His current research interests include RF design and characterization of reconfigurable microwave filters, microwave passive devices, RF microelectromechanical systems, thin-film materials, and additively manufactured RF components.

Dr. Li is also a member of the IEEE Microwave Theory and Techniques Society (IEEE MTT-S), the Chinese Institute of Electronics, and the Applied Computational Electromagnetics Society (ACES). He is also a Reviewer for several IEEE/IET/Wiley/ACES journals and international conferences. He was a co-recipient of the First Place Award at the 2014 and 2015 IEEE MTT-S International Microwave Symposium Tunable RF-MEMS Filter Student Design Competitions.
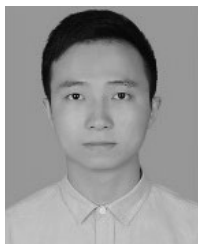
KAI-DONG HONG received the B.E. degree in communication engineering from Guangdong Ocean University, Zhanjiang, Guangdong, China. He is currently pursuing the Ph.D. degree in information and communication engineering with Shenzhen University, Shenzhen, Guangdong.

His current research interests include planar microwave, and millimeter-wave antennas and smart antennas for mobile terminals.

TAO YUAN received the B.E. degree in electronic engineering and the M.E. degree in signal and information processing from Xidian University, Xi'an, Shaanxi, China, in 1999 and 2003, respectively, and the Ph.D. degree in electrical and computer engineering from the National University of Singapore, Singapore, in 2009.

He is currently a Professor with the College of Electronics and Information Engineering, Shenzhen University, Shenzhen, Guangdong, China. His current research interest includes the development of novel RF modules and antennas for mobile terminals and 5G applications.

● ● ●